Self-assembly of Chiral (1R,2S)-Ephedrine and (1S,2S)-Pseudoephedrine into Low-dimensional Aluminophosphate Materials Driven by their Amphiphilic Nature

Beatriz Bernardo-Maestro[a], *Elisa Garrido-Martín*[a], *Fernando López-Arbeloa*[b], *Joaquín Pérez-Pariente*[a] *and Luis Gómez-Hortigüela*[a*]

[a] Instituto de Catálisis y Petroleoquímica, CSIC. C/ Marie Curie 2, 28049. Madrid, Spain.

[b] Departamento de Química Física. Universidad del País Vasco. Apartado 644, 48080-Bilbao, Spain.

Corresponding Author: LGH; Email: lhortiguela@icp.csic.es

Telephone: +34-91-5854785: Fax: +34-91-5854760.

Abstract

In an attempt to promote the crystallization of chiral inorganic frameworks, we explore the ability of chiral (1R,2S)-ephedrine and its diastereoisomer (1S,2S)-pseudoephedrine to act as organic building blocks for the crystallization of hybrid organo-inorganic aluminophosphate frameworks in the presence of fluoride. These molecules were selected because of their particular molecular asymmetric structure, which enables a

rich supramolecular chemistry and a potential chiral recognition phenomenon during crystallization. Up to four new low-dimensional materials have been produced, where the organic molecules form an organic bilayer in-between the inorganic network. We analyze by molecular simulations the trend of these chiral molecules to form this type of frameworks, which is directly related to their amphiphilic nature that triggers a strong self-assembly through hydrophobic interactions between aromatic rings and hydrophilic interactions with the fluoro-aluminophosphate inorganic units. Such self-assembly process is strongly dependent on the concentration of the organic molecules.

Keywords: Aluminophosphate, ephedrine, pseudoephedrine, supramolecular, self-assembly, chirality.

1. Introduction

Homochirality (chirality in its pure enantiomeric form) is ubiquitous in living organisms. Life is built upon asymmetric building blocks, L-aminoacids and D-sugars, which compose the essential biological macromolecules, proteins and nucleic acids.[1,2] As a consequence, the metabolism of living beings distinguishes enantiomers of chiral compounds, very frequently having only one enantiomer the desired therapeutic effect.[3] In this context, the design of chiral solids able to discriminate between enantiomers of a chiral organic compound, either during separation or catalytic processes, represents one of the greatest challenges in contemporary chemical research.[4,5] Although much less frequent, chirality is also expressed in the inorganic world; however, homochirality is extremely rare in this case.[6] Nonetheless, pioneering work demonstrated that these chiral inorganic systems could transfer their chirality to a particular organic process (adsorption or catalysis) resulting in enantioselective operations.[7]

In this context, zeolites and crystalline nanoporous materials in general have been proposed as ideal candidates to achieve an enantioselective-performing chiral solid since they could potentially combine their high surface area and characteristic shape-selectivity with a potential enantioselectivity that might be enhanced by the confinement effect.[8-11] Several chiral zeolites do actually exist.[12-17] However, these nanoporous materials crystallize as racemic crystals (50:50 mixtures of two enantiomorph crystals); nonetheless, there is a very recent example of enantio-enrichment of a chiral zeolite (STW) through the use of rationally-designed chiral organic structure-directing agents.[18]

A particular class of zeolite materials is given by nanoporous aluminophosphates ($AlPO_4$), where SiO_4 tetrahedra are substituted by alternating AlO_4 and PO_4 tetrahedra.[19,20] Recently, the family of 3D nanoporous aluminophosphates with an Al/P ratio of 1 has been increased with the discovery of a number of materials with Al/P ratios lower than 1, giving place to inorganic frameworks built upon 1D-chains, 2D-layers or 3D-structures.[21,22] In these materials, Al can have different coordination environments (AlO_4, AlO_5 or AlO_6), while P is always in tetrahedral coordination, but can have 0, 1, 2 or 3 terminal PO_x groups, imparting to these materials an extremely large compositional and structural versatility. Indeed, a wide range of compositions such as $AlPO_4(OH)^-$, $AlP_4O_{16}^{9-}$, $AlP_2O_8^{3-}$, $Al_2P_3O_{12}^{3-}$, $Al_3P_4O_{16}^{3-}$, $Al_3P_5O_{20}^{6-}$, $Al_4P_5O_{20}^{3-}$, $Al_5P_6O_{24}^{3-}$, $Al_{11}P_{12}O_{48}^{3-}$, $Al_{12}P_{13}O_{52}^{3-}$, $Al_{13}P_{18}O_{72}^{15-}$, has been reported.[22] In particular cases, these low-dimensional framework materials can be transformed into 3D nanoporous aluminophosphates.[23,24]

In the low-dimensional framework materials based on 1D-chains or 2D-layers, the inorganic units are linked by organic molecules, which reside in the space between the inorganic framework, holding the overall structure, and leading to a very rich host-guest chemistry between the organic molecules and the inorganic frameworks, usually

through electrostatic (between the net positive charge of protonated or quaternary ammonium cations and the negatively-charged phosphate groups of the inorganic framework) and H-bond interactions. In this context, the rich and versatile structural chemistry associated to these AlPO frameworks and the rich host-guest chemistry with the organic molecules make these low-dimensional AlPO frameworks ideal candidates where chirality of the organic molecules can be imprinted. Indeed, several chiral low-dimensional frameworks have been reported in the past.[12,25-29]

For an impression of the molecular chirality on the inorganic framework to occur, a strong molecular recognition phenomenon in the host-guest system must be established.

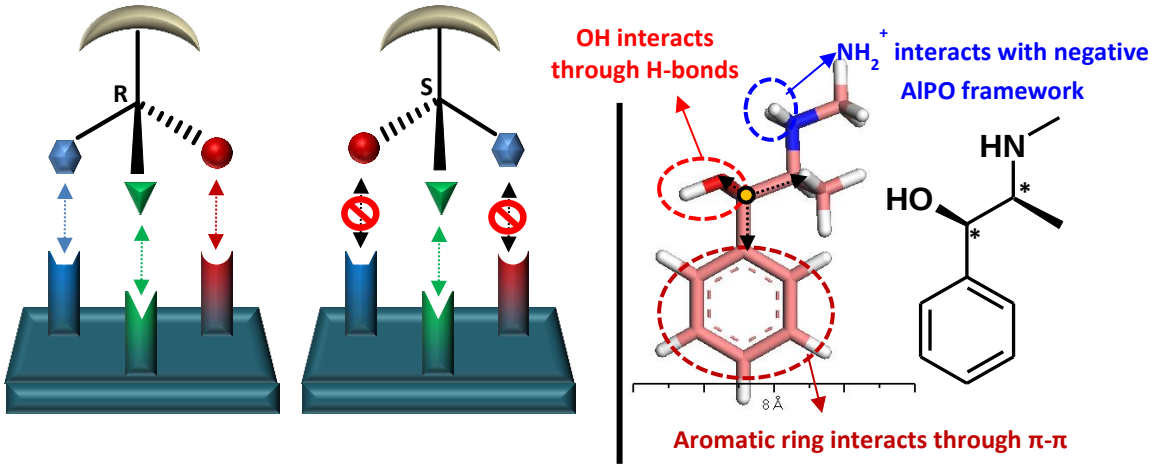

Figure 1. Chiral transfer through 3-point interaction on a 2D-surface (left), and 3-point interaction concept in (1R,2S)-ephedrine.

In this context, the chiral recognition between enantiomers and a nascent chiral surface comprises an intricate cooperative mechanism of spatial molecular complementary recognition which generally involves a three-point specific interaction with several sites on the surface,[30,31] as illustrated in Figure 1 (left). Hence, if we want to reinforce such chiral recognition between the organic molecules and the growing inorganic frameworks, it is convenient to use molecules where the three different substituents (generating a stereogenic center) are susceptible of developing strong and localized interactions with the inorganic surface. Based on this, ideal precursors of chirality

which fulfills all the required conditions to drive the crystallization of aluminophosphate frameworks while enabling such specific interactions are (1R,2S)-ephedrine (Figure 1-right) and its diastereoisomer (1S,2S)-pseudoephedrine. We have studied for some time the structure-directing behavior of these molecules in the synthesis of nanoporous aluminophosphates,[32-34] and we have observed a different supramolecular chemistry behavior driven by their different conformational space.[35] Ephedrine and pseudoephedrine contain two stereogenic centers, one of which has three different substituents able to develop a strong three-point interaction: i) an aromatic ring, which will promote hydrophobic and π-π interactions with other rings, ii) a hydroxyl group which will give place to localized H-bond interactions, and iii) a basic secondary amino group, which will be protonated at the acidic pH of the synthesis, and will develop strong electrostatic and H-bond interactions with the inorganic network (Figure 1-right); indeed, H-bond interactions have been shown to be fundamental for a transfer of chirality to occur.[26] Hence, our purpose was to synthesize new low-dimensional AlPO materials using these chiral molecules as chiral precursors in an attempt to transfer their chirality and imprint it on the inorganic network.

Our previous experience with these molecules[33] showed that high organic and low water contents tend to lead to layered materials with XRD patterns consisting of one intense peak at low angle (4-5º 2θ) corresponding to the basal space. However, no intense peaks in the middle-angle region were observed, suggesting a low ordering of the inorganic framework. In this work we have explored the effect that the addition of fluoride anions has on the crystallization process; in this regard, it is known that fluoride anions facilitate the crystallization of low-dimensional fluoro-aluminophosphate frameworks,[36-55] where fluoride plays a structural role, usually by coordination with Al as bridging or terminal units.

2. Methodology

2. A. Synthesis of crystalline aluminophosphate materials

The synthesis of the different aluminophosphate materials was carried out by hydrothermal methods using (1R,2S)-(–)-ephedrine (EPH) (Sigma Aldrich, 98%) or (1S,2S)-(+)-pseudoephedrine (Sigma Aldrich, 98 %) as organic building blocks. The molar composition of the synthesis gels and the crystallization temperature were systematically varied in order to have pure phases. Low-dimensional aluminophosphate materials were prepared from gels having the following molar composition: 2R:2HF:1P_2O_5:*x*Al_2O_3:50 H_2O, where 'R' was EPH or PsEPH, and '*x*' was 0.5, 0.75 or 1.0. In a typical preparation, the corresponding amounts of H_2O, H_3PO_4 (Sigma-Aldrich, 85 % in water), and pseudoboehmite (Pural SB-1 77.5% Al_2O_3, Sasol), were stirred for 30 minutes. The SDA (EPH or PsEPH) was then added and stirred for 30 minutes. Finally, HF was carefully added and the mixture was stirred for 2 additional hours. The respective gels were introduced into 60 ml Teflon lined stainless steel autoclaves and heated statically at the required temperature (120, 140 or 160 ºC) under autogenous pressure for 24 h. The resulting solids were separated by filtration, washed with ethanol and water and dried at room temperature overnight.

2. B. Characterization

The obtained solids were characterized by powder X-Ray Diffraction (XRD), using a Philips X´PERT diffractometer with CuK_α radiation with a Ni filter. Thermogravimetric analyses (TGA) were registered using a Perkin-Elmer TGA7 instrument (heating rate = 20ºC/min) under air flow. In-situ XRD experiments at increasing temperatures were performed in air from room temperature to 500 ºC (heating rate = 10º/min), collecting XRD data at 50 ºC intervals. Elemental CHN analyses were carried out with a LECO

CHNS-932 elemental analyzer. Field emission scanning electron microscopy (FE-SEM) was carried out on a FEI NOVA NANOSEM 230. Solid State MAS NMR measurements were recorded on a Bruker AV-400-WB spectrometer; details are given in the Supporting Information.

The aggregation state of the molecules within the solid samples was studied by fluorescence spectroscopy. Solid state UV-Visible fluorescence emission spectra were recorded in a RF-5300 Shimadzu fluorimeter. The fluorescence spectra were registered in the front-face configuration by a solid sample holder in which the samples were oriented 30 and 60º with respect to the excitation and emission beams, respectively. Fluorescecence spectra of the solid samples were recorded by means of thin films supported on glass slides ellaborated by solvent evaporation from a CH_2Cl_2 suspension of the solid samples.

2. C. Computational Details

In order to understand the self-assembly of these amphiphilic molecules and relate this to the crystallization of the low-dimensional framework materials, molecular-mechanics simulations were performed. We analyzed the supramolecular aggregation of (1R,2S)-ephedrine and (1S,2S)-pseudoephedrine molecules as a function of the concentration in water solution. Molecular structures of the organic molecules and water were described with the cvff forcefield.[56] Due to the strong basicity of ephedrine (pK_a = 9.6),[57] solutions of protonated EPH and PsEPH chlorides have been studied. The atomic charge-distribution of the protonated cations was obtained from DFT+D calculations, using the B3LYP hybrid functional and the ESP charge calculation method, setting the total net charge to +1. The positive charge of the EPH/PsEPH molecules was compensated by including an equal number of Cl^- anions in the simulations. The atomic charges for the O and H atoms of water molecules were –0.82 and +0.41, respectively.[58]

The aggregation behavior of the molecules in water was studied by means of Molecular Dynamics (MD) simulations, under Periodic Boundary Conditions (PBC), using the Forcite code.[59] 16 protonated molecules and 16 Cl^- anions were included in the simulation cell together with 1600, 800 or 400 water molecules (for relative R:H_2O concentrations of 1:100, 1:50 and 1:25 in the gels, respectively). An initial equilibration period was allowed, consisting of 100 ps of MD simulations in the NPT ensemble at 25 ºC. The density of the systems along this initial MD simulation was averaged, and a frame in the last steps of the MD trajectory with a density close to the averaged value was selected as the starting configuration for the subsequent NVT study. 1000 ps of MD simulations were then run, keeping the temperature constant at 298 K. Of this simulation time, the first 500 ps were assumed as the equilibration period, and only the last 500 ps of the MD simulations were used for data production. The aggregation behaviour of the molecules was studied by analysing the Radial Distribution Functions (RDF) and concentration profiles of different sets of atoms [$g_{\alpha\beta}(r)$]; concentration profiles were calculated according to the following equation:

$$n_{\alpha(\beta)}(r) = 4\pi\rho_\beta \int_0^r g_{\alpha\beta}(r)\, r^2 dr$$

where $n_{\alpha(\beta)}(r)$ is the number of β species surrounding α at less than a given distance (r), ρ_β is the bulk number density of atom β and $g_{\alpha\beta}(r)$ is the α-β RDF.

3. Results

A systematic study of the structure-directing effect of EPH and PsEPH showed that high organic concentrations (with high organic and low water contents) combined with a high fluoride content drove the crystallization pathway towards low-dimensional AlPO materials. Due to the interest in this type of materials where chirality could be

potentially imprinted, we scanned the crystallization of AlPO materials using EPH and PsEPH under these conditions at different Al/P ratios. Results are reported in Table 1.

Table 1. Phase selectivity as a function of the synthesis conditions for gels obtained with composition 2R:2HF:1P_2O_5:*x*Al_2O_3:50 H_2O, with different Al_2O_3 contents. The number of (↑) relates with the crystallinity of the phase.

Experiment	**Al_2O_3**	**R**	**T (ºC)**		
			120	**140**	**160**
EP5	1.0	EPH	EPH-ICP-L1	EPH-ICP-L1(↑)	EPH-ICP-L1(↑↑)
PS5	1.0	PsEPH	PsEPH-ICP-L4(↑)	PsEPH-ICP-L4	PsEPH-ICP-L4
EP6	0.75	EPH	EPH-ICP-L2	EPH-ICP-L2	EPH-ICP-L2(↑↑)
PS6	0.75	PsEPH	PsEPH-ICP-L4	PsEPH-ICP-L4(↑)	PsEPH-ICP-L4
EP7	0.5	EPH	___	EPH-ICP-L3(↑↑)	EPH-ICP-L3(↑)
PS7	0.5	PsEPH	L5+L6	L6+L5	Quartz+dense

Up to six new low-dimensional framework materials have been obtained with EPH (3) and PsEPH (3) in the presence of F, depending on the Al/P ratio in the synthesis gel. EPH led to EPH-ICP-L1 (with an Al/P ratio in the gel of 1, with the highest crystallinity being obtained at 160 ºC), EPH-ICP-L2 (with an Al/P ratio in the gel of 0.75, also with the highest crystallinity at 160 ºC), and EPH-ICP-L3 (with an Al/P ratio of 0.5, with the highest crystallinity observed at 140 ºC); all these samples seem to be pure phases. Figure 2 shows the XRD patterns of these materials. The first diffraction corresponding to the basal space, that we assume as the interlayer distance, was slightly different in the three cases, being 21.8, 20.4 and 19.8 Å for EPH-ICP-L1, -L2 and -L3, respectively (Table 2). Low-angle XRD patterns discarded the occurrence of diffraction peaks at angles lower than 4º 2θ. The XRD patterns of EPH-ICP-L2 and EPH-ICP-L3 are rather similar, although clearly different, especially in the basal space. The same synthesis conditions but using PsEPH lead to distinct materials: in contrast to EPH, both Al/P ratios of 1.0 and 0.75 in the gel lead in this case to a new low-dimensional material, which we denote as PsEPH-ICP-L4, with a basal space of 21.9 Å. Despite being

obtained under the same synthesis conditions (Al/P ratio of 1), EPH-ICP-L1 (obtained with EPH) and PsEPH-ICP-L4 (obtained with PsEPH) have clearly different structures of the inorganic layers, judging by their respective XRD patterns (Figure 2). Again in contrast to the EPH case, an Al/P ratio of 0.5 led to two new low-dimensional materials with PsEPH (L5 and L6), with different relative amounts depending on the synthesis temperature; however, these materials could not be prepared as pure phases, and hence no further characterization was performed.

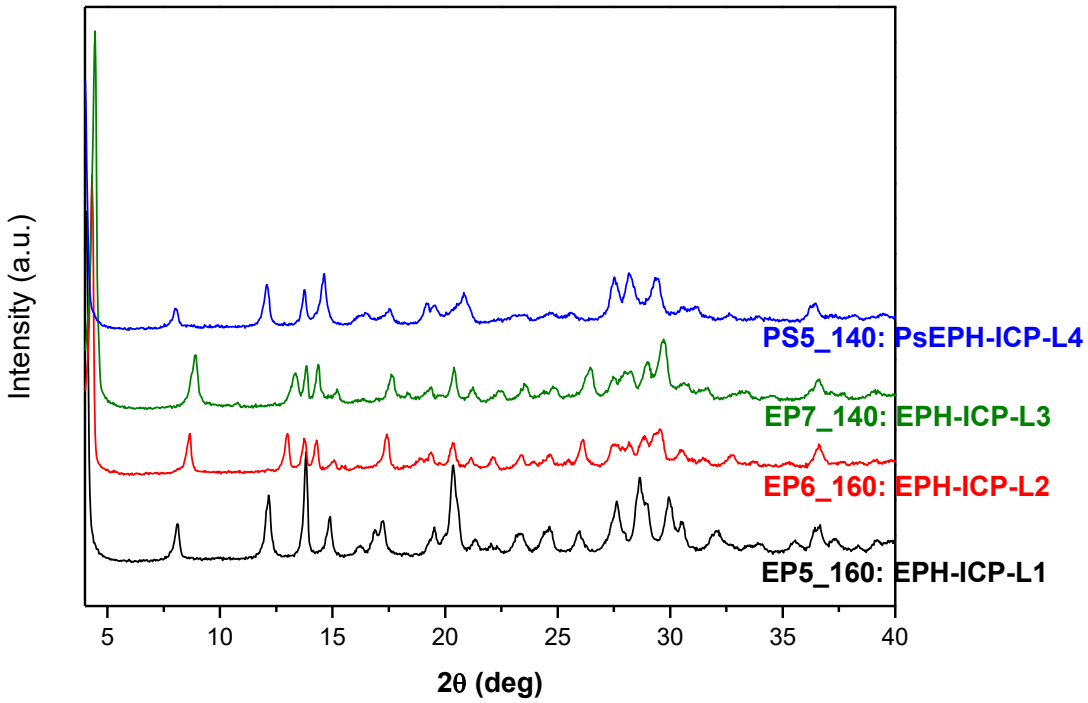

Figure 2. XRD patterns of low-dimensional materials obtained with EPH or PsEPH under different Al/P ratios in the synthesis gel (see Table 1).

Material	SDA	Basal space (XRD)	H_2O % (TGA)	Organic % (CHN)	H_2O % from dihydroxylation
EPH-ICP-L1	EPH	21.8	1.2	49.0	9.8
EPH-ICP-L2	EPH	20.4	3.3	44.2	12.3
EPH-ICP-L3	EPH	19.8	3.4	39.0	13.7
PsEPH-ICP-L4	PsEPH	21.9	1.4	47.6	11.4

Table 2. Properties of the different materials obtained, as determined from XRD, TGA and CHN analyses.

The phase-purity of the different samples was confirmed by FE-SEM (Figure 3): all these materials crystallize as small plates, being those of EPH-ICP-L1 and PsEPH-ICP-L4 (both obtained with an Al/P ratio of 1.0) clearly smaller. In all cases, the SEM images suggest a high purity of the samples.

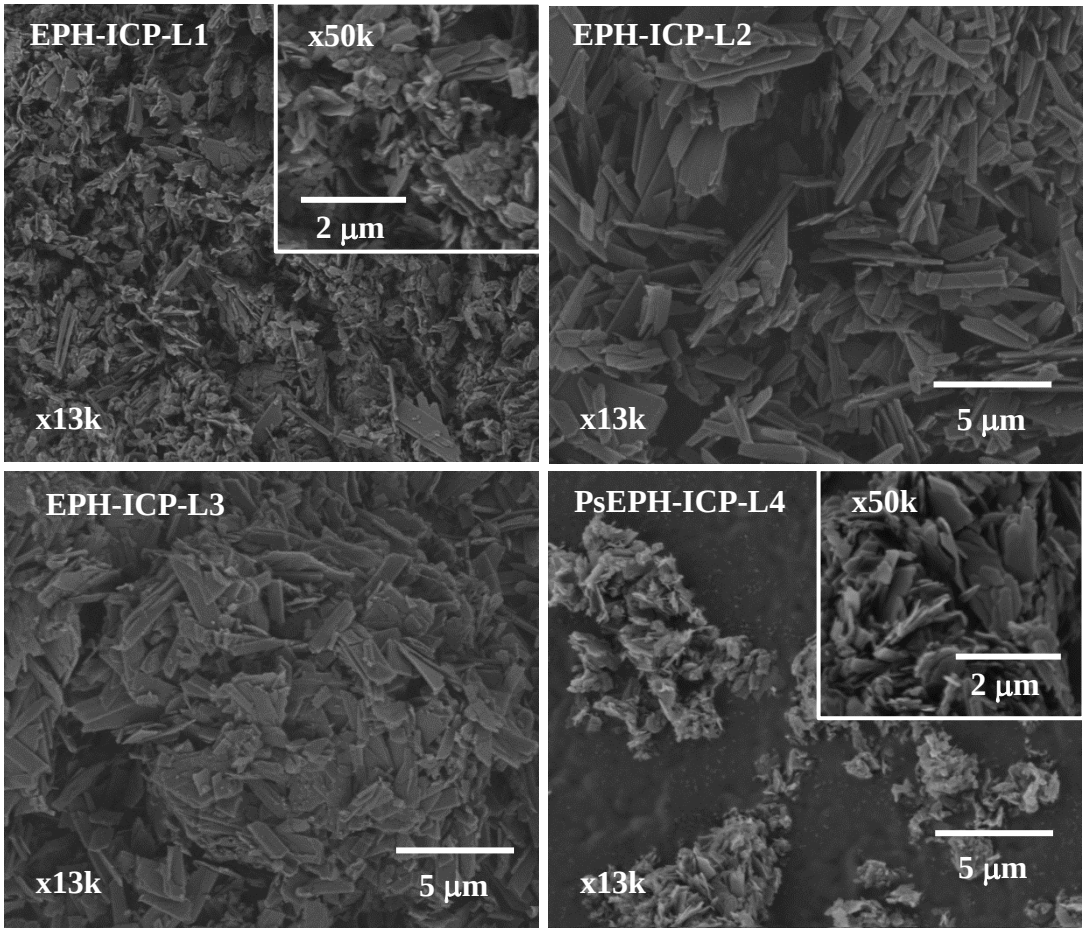

Figure 3. FESEM pictures of the low-dimensional materials obtained with EPH or PsEPH (see Table 1).

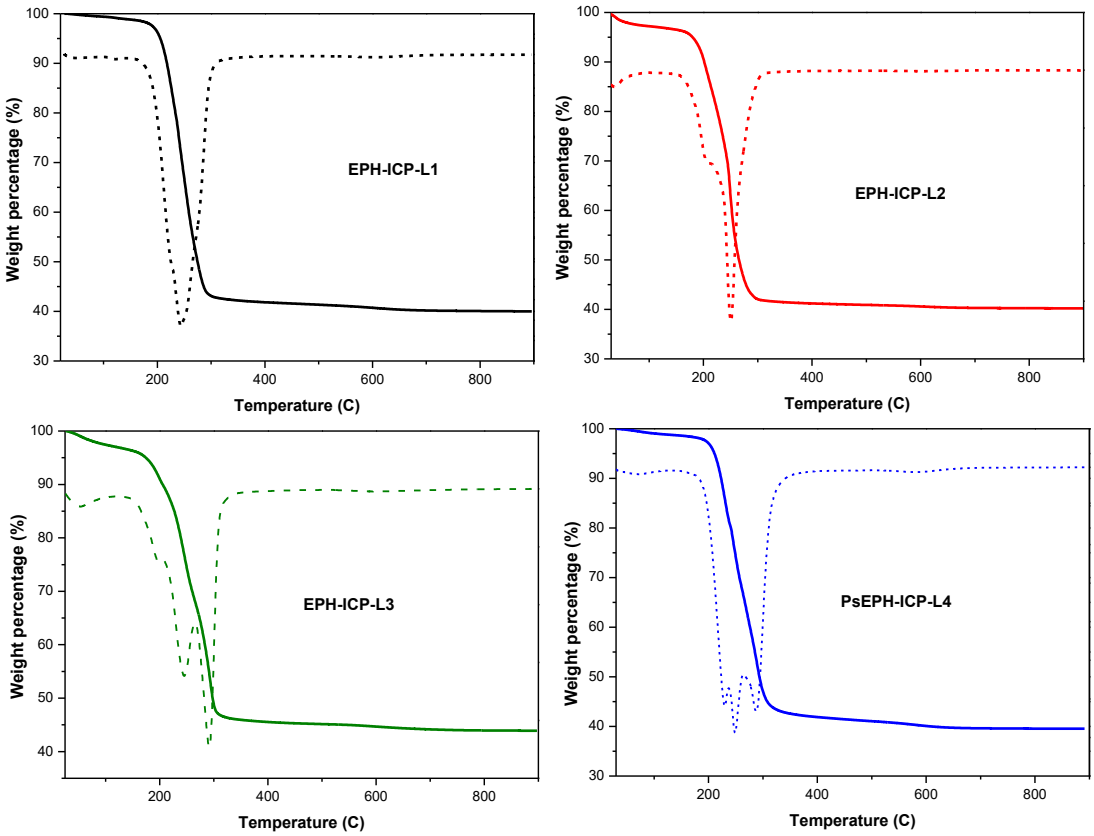

Figure 4. TGA (solid lines) and DTA (dashed lines) of the low-dimensional materials obtained with EPH or PsEPH.

Thermogravimetric analyses are shown in Figure 4; all the low-dimensional materials show a very intense desorption, with weight losses ranging between 50 and 60 % (in the temperature range of 150-900 ºC), with maximum desorption rates between 200 and 300 ºC. EPH-ICP-L1 and PsEPH-ICP-L4, both materials obtained under the same synthesis conditions (Al/P ratio of 1) with the two molecules, show a very low content of physisorbed water (desorption below 150 ºC) (1.2 and 1.4 %, respectively), and similar weight losses between 150 and 900 ºC, being 58.8 and 59.0 %, respectively, with maximum desorption rates at 248 ºC, although the shape of the desorption curve is slightly different. EPH-ICP-L2 and EPH-ICP-L3 show slightly different TGA profiles, with higher contents of physisorbed water (3.3 and 3.4 %, respectively), and slightly lower weight losses at high temperature (56.5 and 52.7 %, respectively), and with

maximum desorption rates at 250 and 290 ºC. Again the shape of the desorption rate is slightly different for these materials.

CHN elemental analyses of the materials showed C/N ratios around 10.2-10.3, very similar to that of the pristine molecules (10), suggesting the integral incorporation of the EPH and PsEPH molecules in the frameworks. The organic contents determined by CHN (calculated from the C %) were extremely large: 49.0, 44.2, 39.0 and 47.6 % for EPH-ICP-L1, EPH-ICP-L2, EPH-ICP-L3 and PsEPH-ICP-L4, respectively (Table 2). These values are smaller than the weight losses observed by TGA between 150-900 ºC, indicating that water is desorbed also in this temperature range, possibly after dihydroxylation processes. Indeed, the amount of water desorbed between 150 and 900 ºC (calculated by the difference between the weight loss observed in the TGA in this temperature range and the organic content found by CHN) was 9.8, 12.3, 13.7 and 11.4 %, respectively (Table 2).

The integrity of the EPH and PsEPH molecules within the different low-dimensional frameworks was confirmed by ^{13}C NMR, where all the resonances corresponding to the different C atoms are observed in all cases (Figure 5). If we compare the three spectra of the materials obtained with EPH, we can see some differences, especially in EPH-ICP-L2 and -L3, with the resonances being broader and some slightly shifted (especially the ones corresponding to C2 and C3). This might point to a different mobility of the molecules in the frameworks and/or to different configurations (possibly different conformations) of the molecules in the interlayer space. Indeed, DFT calculations suggest that the NMR resonances are affected by the different conformations that these molecules can adopt. Hence, it seems that EPH-ICP-L2 and -L3 contain EPH with a conformation different from that in EPH-ICP-L1.

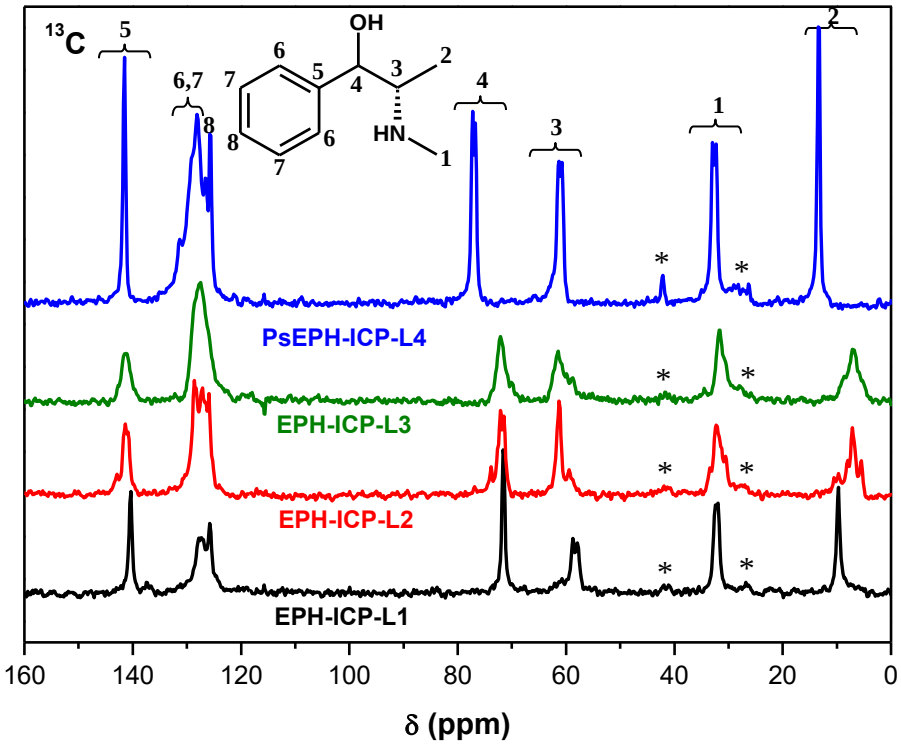

Figure 5. ^{13}C CP MAS NMR of low-dimensional materials obtained with EPH or PsEPH; * designates rotation bands.

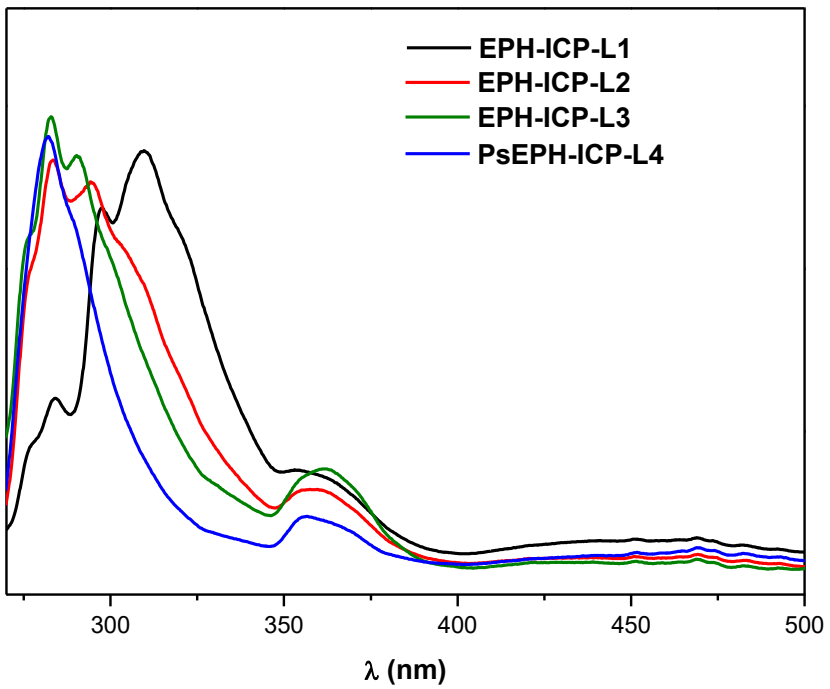

Figure 6. UV-Vis fluorescence spectroscopy of low-dimensional materials obtained with EPH or PsEPH.

Fluorescence spectroscopy of these materials is reported in Figure 6. Unexpectedly, no intense band between 400 and 500 nm, corresponding to strongly π-π stacked dimers,[35] was observed for any of the materials; only EPH-ICP-L1 material showed a slightly higher intensity (but still very low) in this region. A band between 350 and 375 nm was observed in all the materials, suggesting the presence of a minor amount of supramolecular aggregates. The main fluorescence band in EPH-ICP-L2 (red), EPH-ICP-L3 (green) and PsEPH-ICP-L4 was observed at 282 nm, and possessed a vibronic structure; hence, these emission bands were assigned to the molecules arranged as monomers, with no stacking interaction between the aromatic rings. However, EPH-ICP-L1 showed the main band, also with a vibronic structure, red-shifted from the typical 282 nm to 310 nm. The occurrence of the vibronic structure together with the smaller red-shift (with respect to typical π-π stacked dimers which give a higher shift to beyond 350 nm) led us to assign this band to EPH monomers interacting with other monomers in the interlayer space, possibly through coplanar interactions, but no through π-π stacking interactions (these should give a band without vibronic structure and more red-shifted). Hence, these results indicate that the organic bilayer in these materials is not formed by π-π stacking interactions of the aromatic rings.

^{31}P NMR spectra of the materials (Figure S1-left in the Supporting Information) showed bands between -5 and -22 ppm, with the main resonance in all cases at around -10 ppm; indeed, all the materials showed different ^{31}P bands, corresponding to non-equivalent P atoms in the materials. This chemical-shift range is typical of tetrahedral P with two ($PO_{2b}O_{2t}$) or one ($PO_{3b}O_t$) terminal O atoms (O_b are O atoms bridging Al and P tetrahedral atoms, and O_t are terminal O atoms),[60] suggesting that these are the building units of the inorganic frameworks. EPH-ICP-L2 shows up to three different P environments in this band, EPH-ICP-L3 shows at least two, while EPH-ICP-L1 and

PsEPH-ICP-L4 show only one P environment in this band. Furthermore, the two latter samples exhibit two and one additional bands, respectively, at lower shifts, due to P in different environments, possibly with a higher degree of condensation. ^{27}Al NMR spectra (Figure S1-right in the Supporting Information) showed instead broad ill-defined bands between 0 and -60 ppm in all the materials, with different bands and distinct relative intensities for each material, which are assigned to octahedral Al by coordination to O and possibly to F. EPH-ICP-L1 material showed additionally a band at 40 ppm, indicating the presence of tetrahedral Al in this framework.

Finally, the incorporation of F in the low-dimensional materials was evidenced by ^{19}F NMR (Figure S2 in the Supporting Information). All the low-dimensional frameworks showed a very intense ^{19}F resonance at ~-145 ppm, evidencing the incorporation of F to the frameworks. The chemical shift was slightly different: EPH-ICP-L1 and PsEPH-ICP-L4, both prepared with an Al/P ratio of 1, showed a resonance at -145 ppm, while EPH-ICP-L2 and EPH-ICP-L3 showed the band at -146 ppm. F in D4R units gives signals around -90 ppm,[46,39,61] and hence these units can be discarded. In this type of materials, F is usually bonded to octahedral Al in different coordination environments, with F bridging two octahedral Al atoms (F_b) or as terminal F linked to octahedral or tetrahedral Al (F_t).[54] F_b atoms usually give resonances between -110 and -125 ppm.[62-64] In contrast, resonances at ~-143 ppm have been previously assigned to F_t, what suggests that F in our low-dimensional AlPO materials are terminal F bonded to octahedral Al.[55,46] EPH-ICP-L2 and EPH-ICP-L3 showed additionally a band with a very minor intensity at -138 ppm, also due probably to Al-F species, although in these cases it is not clear whether these species belong to the framework or to some other impurities given their very low intensity (compared to the main resonance at -146 ppm).

Layered materials are often precursors to 3D nanoporous materials.[65-69] In an attempt to study the stability of these new materials and analyze the possible transformation into other frameworks, in-situ XRD patterns at increasing temperatures were collected. EPH-ICP-L1 and EPH-ICP-L3 showed a similar behavior (Figure S3 in the Supporting Information): EPH-ICP-L1 was stable up to 150 ºC, and at 200 ºC, where a very intense desorption of organics occurred (as observed by TGA, see Figure 4), the material collapsed and transformed directly into AlPO-trydimite. EPH-ICP-L3 was stable only up to 100 ºC; at 150 ºC, where desorption of volatile compounds just start, the material transforms into something else, the main diffractions of the layers disappear, and some other new diffractions with very low intensity arise at 11.6, 14.7, 18.2 and 29.4º 2θ, while the first diffraction at 4.6 remains (although with a reduced intensity). Further increase of the temperature to 200 ºC, where the main desorption of organics occurs, results again in AlPO-trydimite.

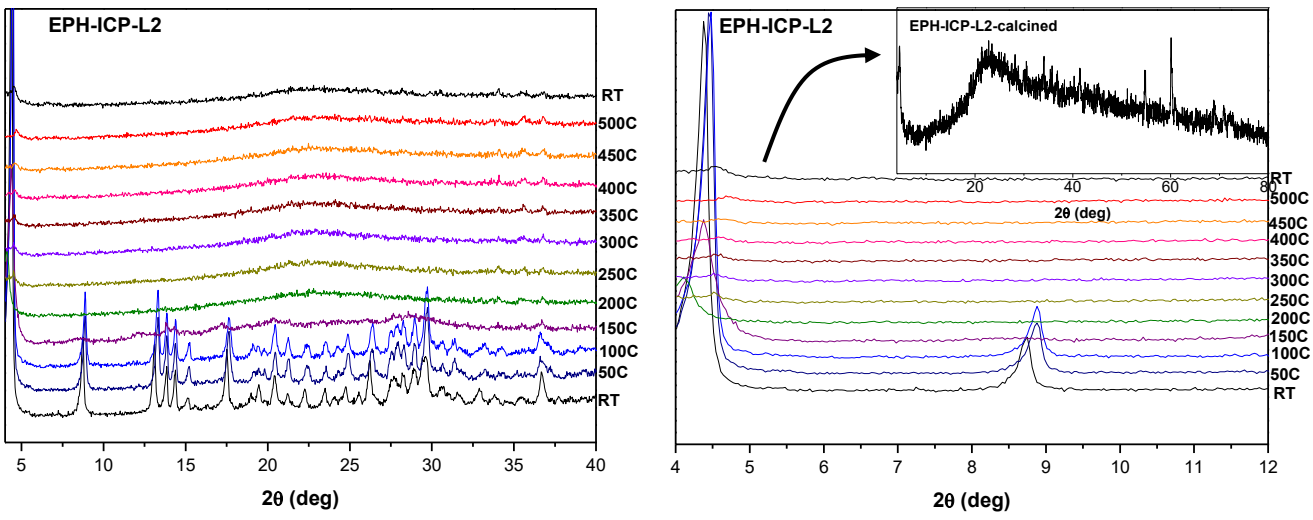

Figure 7. In-situ XRD patterns at increasing temperatures of EPH-ICP-L2 (bottom: detail of the low-angle región); the XRD pattern of the final material after cooling down is shown in the inset.

The behavior of EPH-ICP-L2 with temperature is different, and deserves special attention (Figure 7). In this case, the framework is stable up to 100 ºC. At 150 ºC, the

diffraction corresponding to the basal space at low-angle remains, though with a reduced intensity; however, the rest of diffractions disappear, evidencing a loss of the layer structure of EPH-ICP-L2, while some new broad diffractions arise (purple line). At this temperature, the weight loss is about to start (or even has just started), as observed by TGA (Figure 4). At 200 ºC (green line), where the main weight loss occurs, the first diffraction shifts from 4.4º 2θ (corresponding to a basal space of 20.1 Å) to 4.1º 2θ (corresponding to a basal space of 21.5 Å), evidencing the formation of a distinct phase, though with a lower framework structural order. Further increase of the temperature to 250 ºC shifts back the first diffraction to 4.55 and notably reduces the intensity, and this remains so up to 500 ºC. It is very interesting to note that at 500 ºC, where all the organic matter has been removed (Figure 4), several diffractions remain (though with very low intensity), remarkably such first diffraction now at 4.7º 2θ, but also other minor diffractions at 35.8, 36.9, 41.5, 54.9 and 60.2º 2θ, evidencing the formation of a new material with a very large basal space, although in a very minor concentration with respect to the amorphous material. When cooled down, this new material remains stable (Figure 7-right). This is an interesting observation since we should keep in mind that the material is now organic-free, and hence the inorganic network cannot be held by the organic bilayer; therefore a stable-to-calcination 3D AlPO framework must have been produced from EPH-ICP-L2. Work is now currently under way in an attempt to isolate this new material with a higher crystallinity.

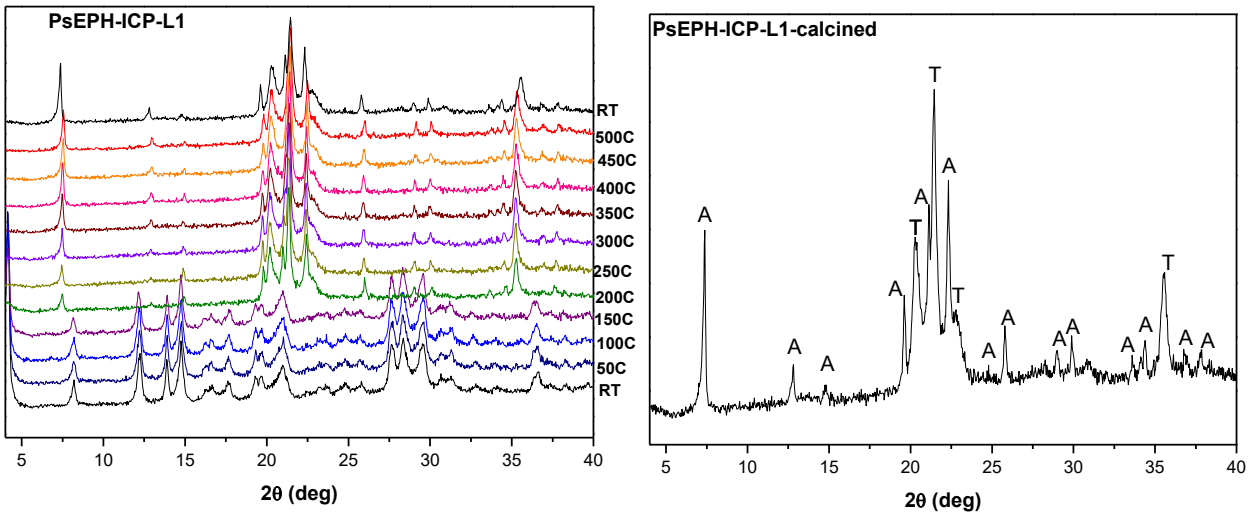

Figure 8. In-situ XRD patterns at increasing temperatures of PsEPH-ICP-L4 (left); right: XRD pattern of the final material after cooling down, where 'A' indicates AFI diffractions, and 'T' stands for AlPO-trydimite diffractions.

Finally, in-situ XRD study of PsEPH-ICP-L4 also led to an interesting behavior (Figure 8). In this case, the material is stable up to 150 ºC (purple line). At 200 ºC, PsEPH-ICP-L4 collapses and a mixture of AlPO-trydimite and AlPO-5 (AFI-type structure) appears. With further heating, the intensity of the diffractions of AFI increases. When cooled down (Figure 8-right), the mixture of AlPO-5 and AlPO-trydimite remains. These results suggest that the framework of PsEPH-ICP-L4 must be structurally related to that of the AFI framework, as has been already observed in other layered materials.[70]

Based on the present work and our previous experience in the study of the structure-direction of these molecules, we have observed that the crystallization of this type of low-dimensional materials is clearly dependent on the concentration of the organic molecules: these materials only crystallize under very high organic concentrations. The very large basal space (around 20-22 Å) and the extremely high organic contents (around 40-50 %) of the four materials obtained, combined with the amphiphilic nature of the organic molecules, point to low-dimensional frameworks where the inorganic

low-dimensional frameworks are held together by a bilayer of the organic molecules. The occurrence of this organic bilayer is driven by the supramolecular aggregation trend of EPH and PsEPH, although fluorescence spectroscopy clearly shows that no π-π stacking of the aromatic rings occur, and hence a more disordered supramolecular aggregation of the molecules in the organic bilayer should occur.

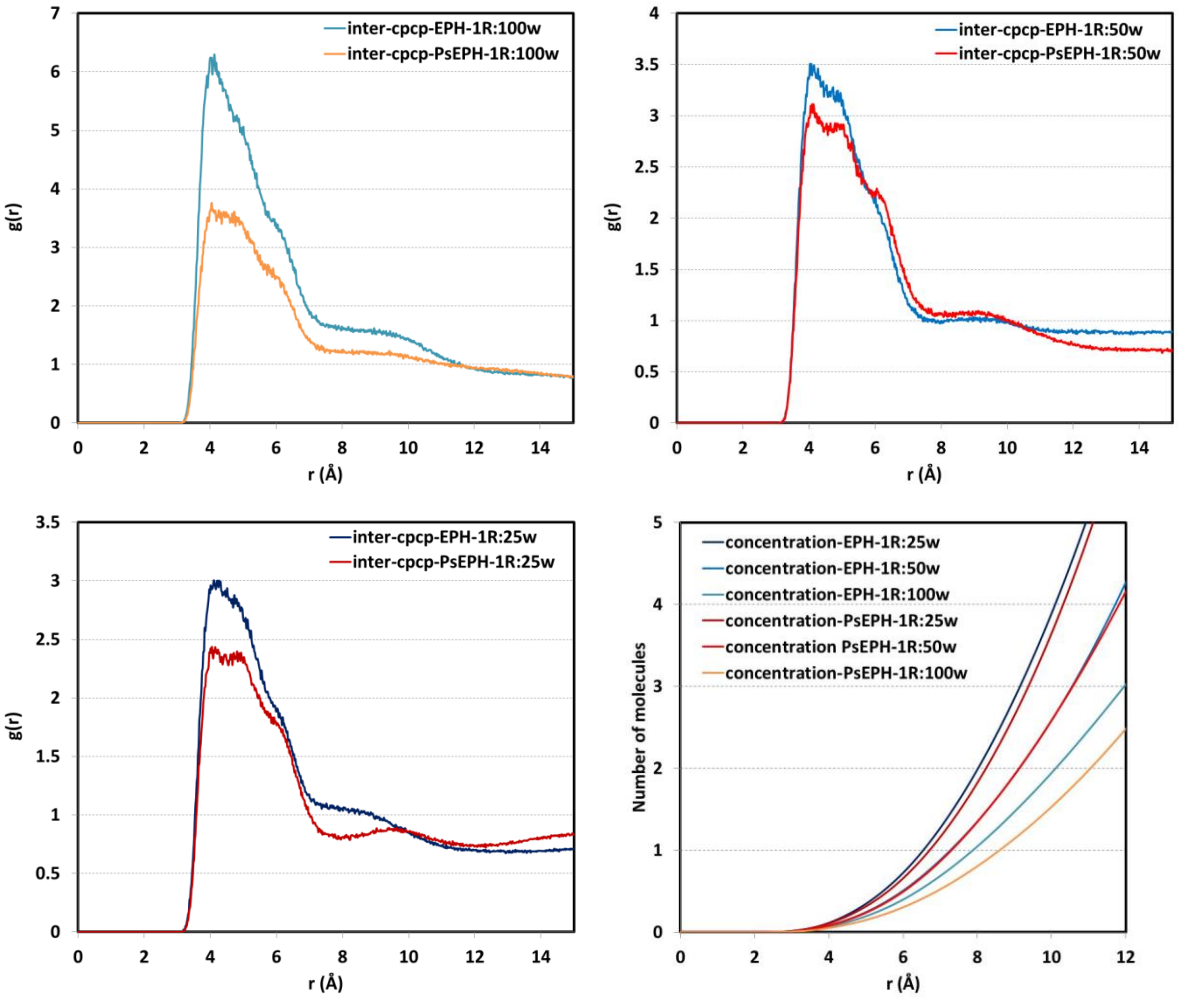

Figure 9. RDF between aromatic C atoms at different concentrations for EPH (blue lines) and PsEPH (red lines) (top, and bottom-right), and concentration profile of organic molecules (bottom-left).

Computational results

We then performed a Molecular Dynamics study in order to understand the supramolecular aggregation of EPH and PsEPH as a function of the concentration,

which at the end results in the crystallization of the different materials. As in our previous works,[35] the supramolecular aggregation of the molecules through the aromatic rings was analyzed by looking at the RDFs between the aromatic C atoms (Figure 9); peaks between 4 and 6 Å are indicative of the formation of this type of aggregates. As observed in our original work,[35] the aggregation of EPH at 1R:100H_2O concentration is much higher than that of PsEPH (Figure 9-top-left). This is due to the configuration of PsEPH (with both asymmetric C atoms in '*S*' configuration), which involves a particular conformational space led by the development of intramolecular H-bonds, different from that of EPH with a distinct diastereomeric configuration. There are two types of stable conformations in these molecules, with an open- or folded-configuration (see Figure 10-top-left). The occurrence of these two conformations can be monitored by plotting the RDF between the aromatic C atom with the substituent attached (labelled as 'cp1') and the terminal methyl group bonded to N ('c3n'). At a concentration of 1R:100H_2O (Figure 10-top-right), we can clearly observe the presence of two peaks (with similar intensity) in these RDFs for PsEPH (orange line), evidencing the occurrence of the two conformations for PsEPH at this concentration, the open-configuration (with the alkyl chain extended, peak at 5.0 Å) and the folded-configuration (with the alkyl chain folded, peak at 3.7 Å), as we reported previously.[35] The latter configuration prevents the formation of aggregates because of steric hindrance, thus reducing the supramolecular aggregation behavior of this diastereoisomer (Figure 9-top-left). In contrast, EPH only occurs in an open-configuration (Figure 10-top-right, light blue) which is compatible with the formation of aggregates, and hence its supramolecular aggregation is higher. In this case, the occurrence of two peaks at 4.7 and 5.0 Å is due to the rotation of the terminal N-CH_3 group, but preserving the open-configuration.

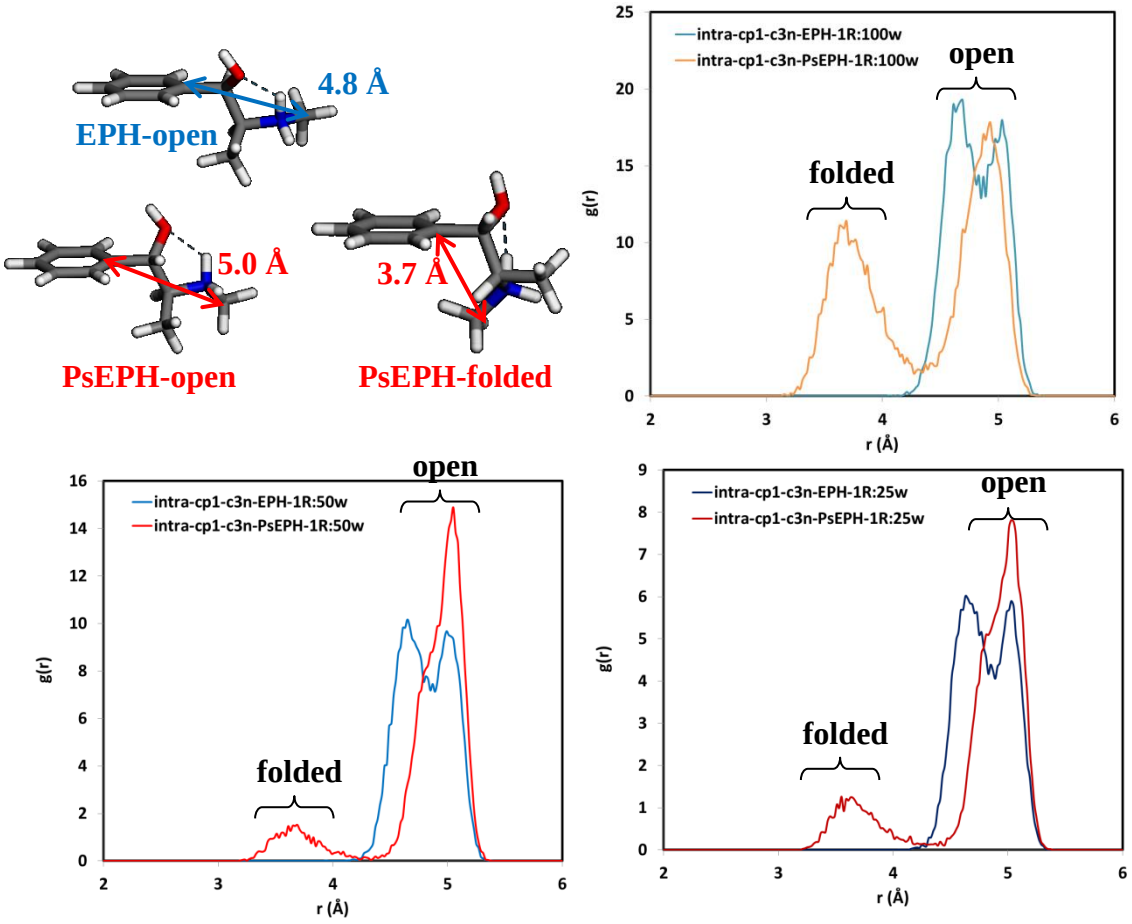

Figure 10. RDF between cp1 and c3n atoms (see pictures), distinguishing the occurrence of the different conformations, at different concentrations for EPH (blue lines) and PsEPH (red lines).

Interestingly, when we increase the concentration to 1R:50H_2O, the difference in the supramolecular aggregation of the two diastereoisomers is notably reduced, being now only slightly higher that of EPH, as indicated by the RDFs between aromatic C atoms (Figure 9-top-right). At this concentration, EPH still only occurs as conformers with open configuration (peaks around 4.8 Å); however, PsEPH shows a behavior different than that at lower concentration (1R:100H_2O), where the conformation with the open-configuration is now clearly much more abundant (Figure 10, bottom-left, red line). Indeed, a similar picture is observed upon a further increase of the concentration to 1R:25H_2O, where again the difference in the supramolecular behavior between the two diastereoisomers is small (Figure 9, bottom-left) (though with EPH always displaying a

slightly stronger supramolecular aggregation), and again this is due to the low occurrence of the folded-configuration for PsEPH at this high concentration (Figure 10, bottom-right). Therefore, these results suggest that the concentration of the organic molecules can in turn alter the supramolecular aggregation of self-assembling molecules, not only by altering the probability of finding other molecules (this of course is expected: higher concentrations of the self-assembling species lead to stronger aggregations), but also by altering the conformational behavior of the molecules.

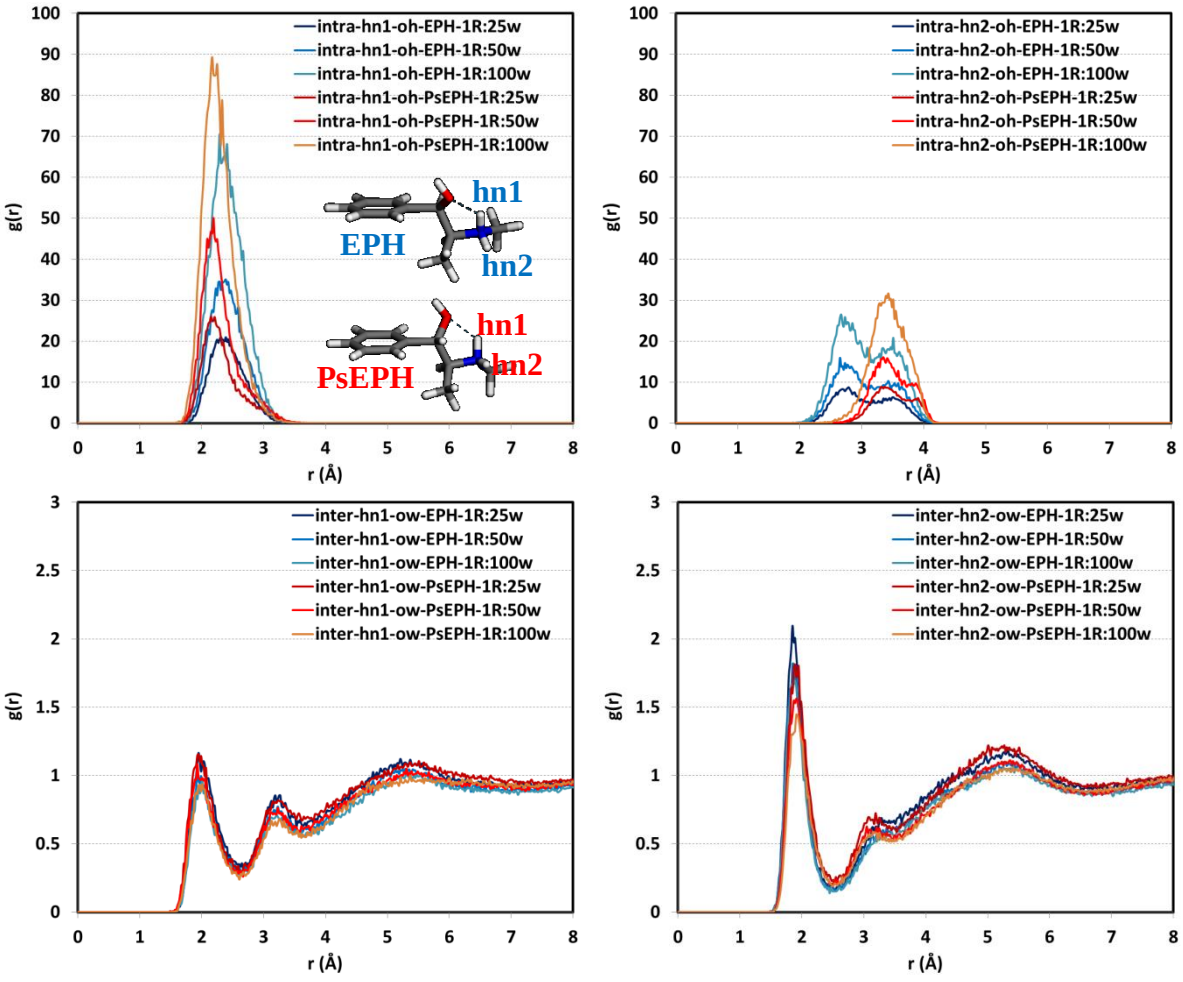

Figure 11. Top: intramolecular RDFs between the two molecular H(N) (left and right) and O atoms for EPH (blue lines) and PsEPH (red lines); bottom: intermolecular RDFs between the two molecular H(N) and water O atoms for EPH (blue lines) and PsEPH (red lines).

Such aggregation is driven by the hydrophobic nature of the aromatic rings. We then analyzed the H-bond interactions of the polar groups of the molecules. In both diastereoisomers, there are two H-bonded-to-N atoms (H-bond donor groups) able to develop intramolecular or intermolecular H-bonds (labelled as 'hn1' and 'hn2' in Figure 11, top-left). Intramolecular RDFs between these hn atoms and O atoms (of EPH and PsEPH) reveal that intramolecular H-bonds are always developed with 'hn1' (top-left) and not with 'hn2' (top-right), regardless of the diastereoisomer and of the concentration. This preferential H-bond formation (with just one of the two possible H(N) atoms) strengthens the asymmetric nature of these chiral molecules through a reduction of the molecular flexibility and hence of the conformational space. Water molecules interact more strongly with 'hn2' atoms through intermolecular H-bonds (peak at 1.9 Å, Figure 11, bottom-right) in all cases (both EPH and PsEPH at the different concentrations) than with 'hn1' atoms (Figure 11, bottom-left). In this context, a similar asymmetric strong interaction of these 'hn2' atoms with PO_4 anionic groups could be expected during crystallization of the low-dimensional frameworks, enhancing the chance of imprinting the molecular chirality on the inorganic framework.

We then analyzed the different types of (hydrophilic/hydrophobic) interactions. The high trend of this type of molecules to form supramolecular aggregates is due to their amphiphilic nature: on the one hand, they contain a hydrophobic aromatic ring that tends to self-assemble through hydrophobic and π-π interactions with other aromatic rings, avoiding the contact with water molecules, as evidenced by the absence of strong interactions of the aromatic H atoms with water molecules (Figure 12, top-left); hence these aromatic rings locate towards the center of the aggregates (forming a kind of 'core'), stabilized by hydrophobic interactions. On the other hand, they also contain polar groups on the other side of the molecule which strongly interact with water

molecules through H-bond interactions, both the H(O) atoms with water O atoms (Figure 12-bottom-left), and the H(N) atoms with water O atoms (Figure 12-top-right). The interaction of O(H) atoms of the organic molecules with water H atoms is much more restricted (Figure 12-bottom-right), which is explained since O atoms are already involved in intramolecular H-bonds with 'hn1'. Therefore, the ammonium and hydroxyl groups will locate at the borders of the aggregates in contact with the water molecules, forming the shell of the aggregates.

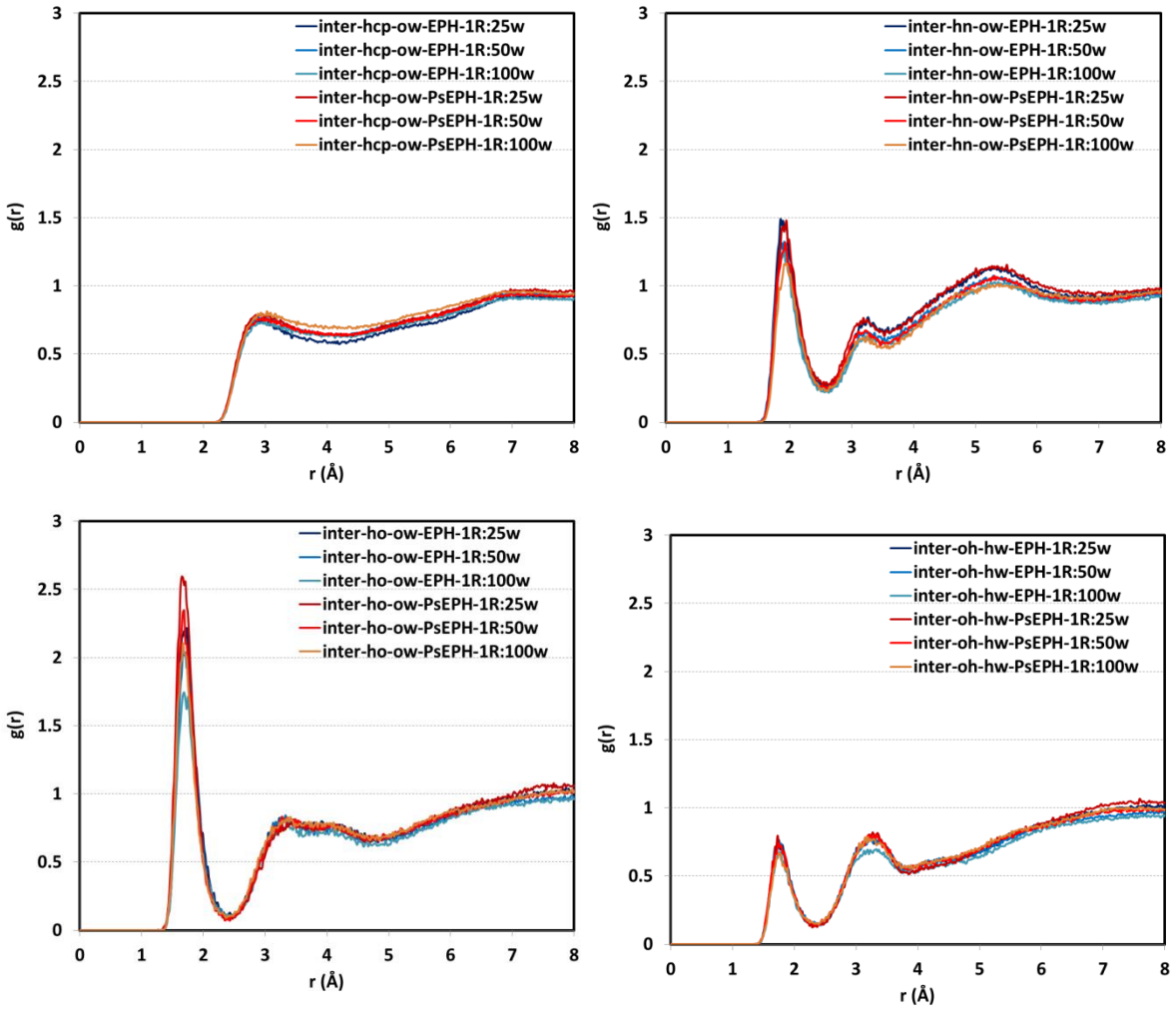

Figure 12. RDF between different atoms of the SDA molecules and water atoms. Top-left: between aromatic H atoms and water O atoms; top-right: between H(N) atoms and water O atoms; bottom-left: between H(O) atoms and water O atoms; bottom-right: between O(H) atoms and water H atoms.

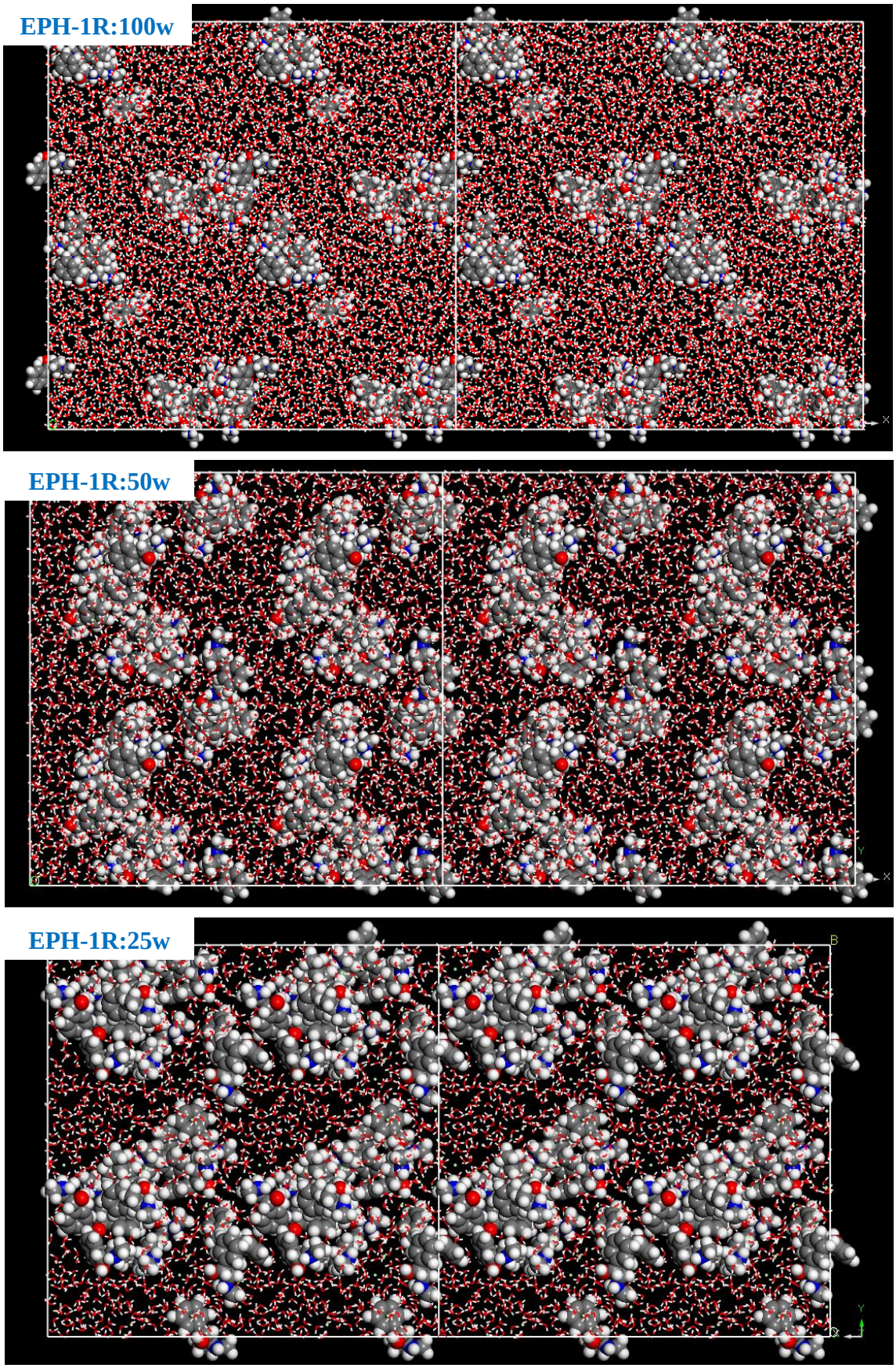

Figure 13. Snapshot (MD t = 1000 ps) of the aggregation of EPH at the different concentrations; EPH molecules are shown as CPK models, and water molecules as line models.

We finally analyzed the size of the supramolecular aggregates as a function of the

concentration in order to understand the trend of low-dimensional frameworks to crystallize only from highly concentrated gels. The size of the supramolecular aggregates can be analyzed by the concentration profiles, which are calculated from the corresponding RDFs, as explained in the experimental section. Figure 9 (bottom-right) shows the concentration profiles of the organic molecules surrounding a given one, as a function of the concentration; the number of organic molecules at less than a particular distance is an indication of the molecular coordination environment, which can be used as an estimation of the aggregates size. If we focus for instance at a distance of 8 Å, we observe that 0.8 molecules surround a given one for PsEPH at 1R:100H_2O concentration; this number is increased to 1.0 for EPH, as a consequence of its higher aggregation trend. This indicates that the size of the aggregates is not very large, as can be seen from the snapshot of the MD simulations (see Figure 13-top). An increase of the concentration to 1R:50H_2O increases the size of the aggregates: we now have 1.4 molecules for both EPH and PsEPH (Figure 9-bottom-right); in this case, the size of the aggregates is larger, but still we can appreciate discrete supramolecular clusters (see Figure 13, middle). Finally, a further increase of the concentration to 1R:25H_2O notably increases the size of the aggregates, having now 1.8 and 2.0 molecules for EPH and PsEPH, respectively (Figure 9-bottom-right). In fact, we now do not see discrete clusters (of different size) as in the previous concentrations, but we now observe a roughly continuous organic phase segregated from water, leading to very large organic aggregates (see Figure 13-bottom; Figure S4 in the Supporting Information shows the corresponding aggregates for PsEPH molecules). Such differences observed in the size of the supramolecular aggregates can explain the trend of these molecules to form layered-like materials under very high concentrations, due to the formation of segregated phases, in a similar way as the formation of bilayers of surfactant molecules.

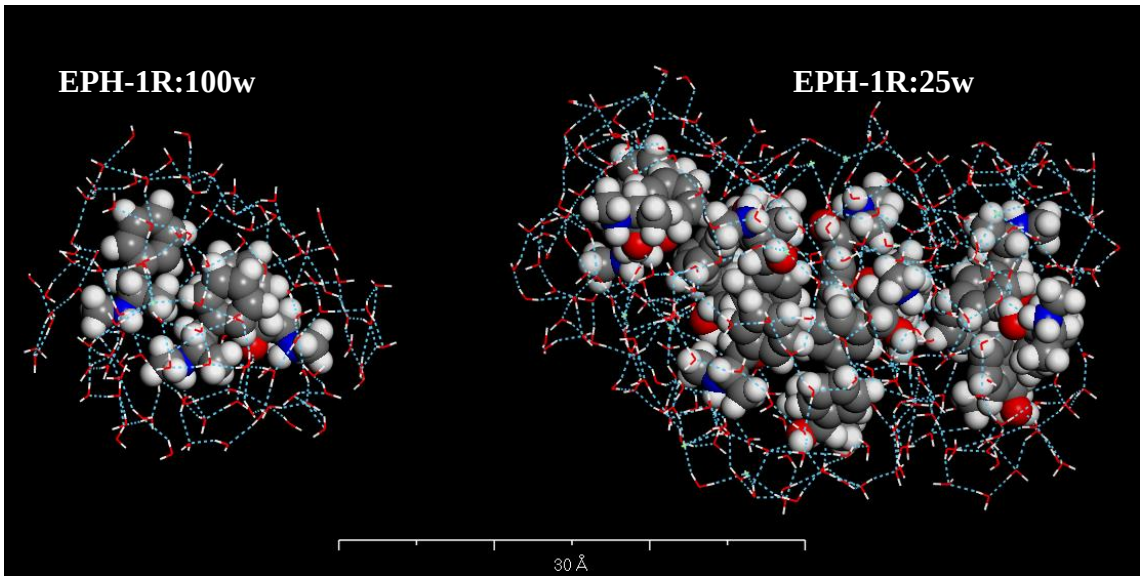

Figure 14. Snapshot (MD t = 1000 ps) of typical aggregates of EPH (shown as CPK models) at two concentrations; only water molecules (shown as sticks) at a radical distance from the organic atoms below 5 Å are shown.

Figure 14 shows the structure of two aggregates typically found during the MD simulations at 1R:100H_2O and 1R:25H_2O, where we can clearly observe the different size as a function of the concentration. We can also appreciate the core-shell-like structure of the large aggregates, with the polar groups (N in blue and O in red) in the shell in close interaction with water and the aromatic rings in the core stabilized by hydrophobic interactions. Hence, it becomes clear that the two types of interactions, hydrophobic on one side and hydrophilic on the other, and hence the amphiphilic nature of these molecules, drive the formation of large supramolecular aggregates in water solution at high concentration in a similar fashion as the behavior of surfactant micellar arrangements.

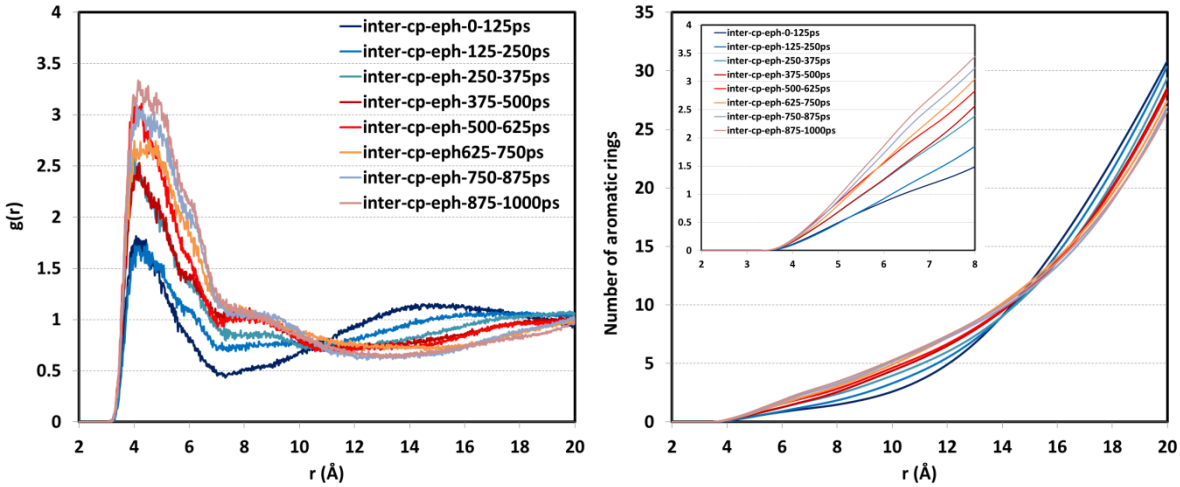

Figure 15. Evolution of the RDF between aromatic C atoms (calculated in different time intervals) (left) and of the corresponding concentration profiles (right) for EPH at 1R:25H_2O composition.

We finally analyzed the evolution of the self-assembly procedure of these amphiphilic molecules to form the large aggregates at the highest concentration along the simulation time. Figure 15 shows the RDF between aromatic C atoms in different time intervals (for EPH; the corresponding results for PsEPH are shown as Figure S5 in the Supporting Information). We can clearly observe that at the beginning of the simulation (from 0 to 125 ps, dark blue line), there is a peak at ~4 Å indicative of the formation of aggregates (Figure 15-top-left). The molecular coordination number (at a distance of 6 Å, Figure 15-top-right) is 0.92 molecules, suggesting the formation of dimers (2-molecules aggregates); indeed, there is a broad peak at 14 Å in the RDF which is consistent with the limited aggregation and the small aggregate size. Evolution of the system with the simulation time leads to a progressive increase of the peak at 4 Å (and a consequent decrease of the peak at 14 Å), clearly evidencing an enhancement of the aggregation and hence a self-assembly of the molecules into larger aggregates through hydrophobic interactions. Indeed, the molecular coordination environment progressively increases from 0.92 (at 0-125 ps interval) up to 1.86 (at the final 875-1000ps interval)

molecules; such evolution of the self-assembly procedure is depicted in Figure S6 in the Supporting Information. A similar self-assembly procedure is observed for PsEPH molecules (Figure S5 in the Supporting Information), although in this case the aggregation is slightly less intense.

Finally, the evolution of the structure of the aggregates is analyzed by comparing the RDF between cp4 (aromatic C atoms in para position) and cp1 (aromatic C atoms with the substituent attached) (Figure 16). The evolutions of the corresponding RDFs are rather different, being much more intense for cp4 atoms than for cp1. At the beginning of the simulation, both RDFs are similar, suggesting that the aromatic rings of the aggregates are parallel (efficient π-π stacking). However, in the final aggregates, the RDF between the cp4 atoms shows a much more intense peak than for cp1, suggesting that the aromatic rings are not perfectly (parallel) stacked, but instead there is a strong hydrophobic interaction between the cp4 atoms (located in the core of the aggregates). This could explain the lack of π-π stacked aggregates observed by fluorescence spectroscopy, while still the aggregation through hydrophobic interactions being very intense, as experimental results suggest.

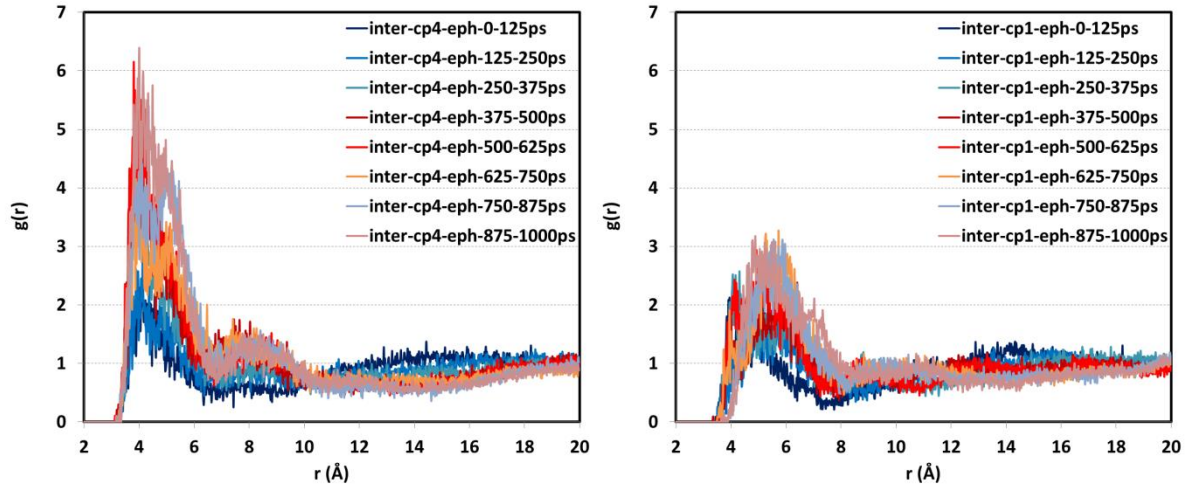

Figure 16. Evolution of the RDF between aromatic C atoms in para position (cp4, left) or in position with C attached (cp1, right), calculated in different time intervals for EPH at 1R:25H_2O composition.

Discussion

In this work we show the synthesis and characterization of four new low-dimensional materials crystallized in the presence of the chiral amphiphilic molecules (1R,2S)-ephedrine and (1S,2S)-pseudoephedrine. The aromatic rings of these molecules tend to interact through hydrophobic interactions, resulting in a self-assembly procedure which leads to the formation of core-shell aggregates, with the core stabilized by hydrophobic interactions between the aromatic rings and the shell occupied by the polar ammonium and hydroxyl groups surrounded by water molecules through hydrophilic interactions. The size of these aggregates is dependent on the concentration of the organic molecules, and very high concentrations lead to continuous organic bilayer aggregates which will compose the interlayer space in the low-dimensional AlPO frameworks. It is expected that the water molecules interacting with the hydrophilic shell of such supramolecular aggregates will be replaced by the ionic $AlPO_x$ units which will compose the inorganic framework, interacting through electrostatic interactions with the positively-charged ammonium groups. The presence of fluoride in the gels facilitates the formation of a well-ordered inorganic network, while in its absence a similar layer-like material is formed, with a similar organic bilayer, but where the inorganic framework is less ordered (the XRD pattern of this material shows only a diffraction peak at low angle corresponding to the basal space). Depending on the relative amount of Al and P in the gel, up to three different materials with each chiral molecule can be prepared. Despite not displaying π-π stacking, as observed by fluorescence, we propose that these materials will display an organic bilayer with supramolecular aggregates in the interlayer space stabilized by hydrophobic interactions. In fact, this has been already observed in the literature: in $[AlPO_4(OH)](NH_3C_2H_4C_6H_5)$, obtained with an aromatic

amine,[71] the interlayer space is composed with an organic bilayer without π-π stacking (see Figure S7 in the Supporting Information). Note that the interlayer separation in this material is ~20 Å, very close to the ones found in our materials, and therefore we expect a similar structure.

The two diastereoisomers show a different conformation behavior which leads to a different supramolecular aggregation trend. However, it is interesting to note that such conformational space is dependent on the concentration of the chiral molecules: an increase of the concentration of PsEPH molecules reduces the formation of the folded aggregation-preventing configuration. Indeed, under high concentrations, both EPH and PsEPH are stable in the open-configuration and develop very strong intramolecular H-bonds between O atoms of the hydroxyl groups and one particular H atom bonded to N (hn1) because of steric reasons. Indeed, if these conformations are preserved in the inorganic framework, the main interaction of this AlPO framework with the organic molecules residing in the interlayer space should be through the negatively-charged PO_4 groups and the positively-charge free H (hn2) atoms, through strong H-bond interactions; therefore, this asymmetric interaction could facilitate the transfer of chirality from the organic molecules to the inorganic framework. Work is currently under way in an attempt to solve the crystalline structure of the four new materials.

Conclusions

Four new fluoroaluminophosphate framework materials have been obtained using chiral (1R,2S)-ephedrine and (1S,2S)-pseudoephedrine as organic building blocks. These materials crystallize in the presence of fluoride, which facilitates the formation of the inorganic network, under high organic and low water contents. These low-dimensional materials contain a fluoro-aluminophosphate inorganic network, mainly with Al in

octahedral coordination with O and F atoms, and tetrahedral P with some terminal O atoms; these inorganic units are held together by an organic bilayer formed by the chiral molecules stabilized by hydrophobic interactions but not through π-π stacking. Some of these materials transform into other potentially interesting phases upon calcination.

MD simulations show that the lower supramolecular aggregation trend of pseudoephedrine (caused by its distinct conformational space) is cancelled upon an increase of the concentration since now the formation of the aggregation-preventing folded-conformer is minor. Our molecular simulations show that the self-assembly behavior of these molecules into supramolecular aggregates is driven by the amphiphilic nature of the organic units, and is strongly dependent on their concentration: high concentrations of the organic molecules lead to larger aggregates with a core-shell structure, where the core is composed by the aromatic rings stabilized through hydrophobic interactions, and the shell is occupied by the hydrophilic ammonium and hydroxyl groups which will strongly interact with the inorganic network.

Supporting Information

In-situ XRD, NMR spectra, and molecular pictures are included as Supporting Information.

Conflicts of interest

There are no conflicts of interest to declare.

Acknowledgements

This work has been partially financed by the Spanish Ministry of Economy, Industry and Competitiveness (Project MAT2015-65767-P) and the Spanish State Research

Agency (Agencia Española de Investigación, AEI) and the European Regional Development Fund (Fondo Europeo de Desarrollo Regional, FEDER) through the Project MAT2016-77496-R (AEI/FEDER, UE). BBM acknowledges the Spanish Ministry of Economy and Competitivity for a predoctoral (BES-2013-064605) contract. Secretaría General Adjunta de Informática-CSIC is acknowledged for running the calculations, and BIOVIA for providing the computational software.

References

(1) M. Gardner, The Ambidextrus Universe. Symmetry and Asymmetry from Mirror Reflections to Superstrings, 3rd Revised, Penguin Books, 1964.

(2) W. J. Lough and I. W. Wainer, Chirality in Natural and Applied Science. ISBN 9780849324345. Blackwell (2002).

(3) M. Rouhi, *Chem. Eng. News.*, 2005, 883.

(4) D. Dubbledam, S. Calero and T. J. H. Vlugt, *Molec. Sim.*, 2014, **40**, 585-598.

(5) K. D. M. Haris and S. J. M. Thomas, *ChemCatChem.*, 2009, **1**, 223-231.

(6) R. M. Hazen and D. S. Sholl, *Nat. Mater.*, 2003, **2**, 367-374.

(7) P. R. Kavasmaneck and W. A. Bonner, *J. Am. Chem. Soc.*, 1977, **99**, 44-50.

(8) T. S. Van Erp, T. P. Caremans, D. Dubbeldam, A. Martín-Calvo, S. Calero and J. A. Martens, *Angew. Chem. Int. Ed.*, 2010, **49**, 3010-3013.

(9) J. M. Castillo, T. J. H. Vlugt, D. Dubbeldam, S. Hamad and S. Calero, *J. Phys. Chem. C*, 2010, **114**, 22207-22213.

(10) M. E. Davis, *Top. Catal.*, 2003, **25**, 3-7.

(11) R. E. Morris and X. H. Bu, *Nat. Chem.*, 2010, **2**, 353-361.

(12) J. Yu and R. Xu, *J. Mat. Chem.*, 2008, **18**, 4021-4030.

(13) M. M. J. Treacy and J. M. Newsam, *Nature*, 1988, **332**, 249-251.

(14) N. Rajic, N. Z. Logar and V. Kaucic, *Zeolites*, 1995, **15**, 672-678.

(15) J. Sun, C. Bonneau, A. Cantín, A. Corma, M. J. Díaz-Cabañas, M. Moliner, D. Zhang, M. Li and X. Zou, *Nature*, 2009, **458**, 1154-1157.

(16) A. Rojas and M. A. Camblor, *Angew. Chem. Int. Ed.*, 2012, **51**, 3854-3856.

(17) L. Q. Tang, L. Shi, C. Bonneau, J. L. Sun, H. J. Yue, A. Ojuva, B. L. Lee, M. Kritikos, R. G. Bell, Z. Bacsik, J. Mink and X. D. Zou, *Nat. Mater.*, 2008, **7**, 381-385.

(18) S. K. Brand, J. E. Schmidt, M. W. Deem, F. Daeyaert, Y. Ma, O. Terasaki, M. Orazov and M. E. Davis, *Proc. Natl. Acad. Sci.*, 2017, **114**, 5101-5106.

(19) S. T. Wilson, B. M. Lok, E. M. Flanigen, U.S. Patent 4,310,440, 1982.

(20) R. Szostak, Molecular Sieves, Principles of Synthesis and Identification. Blackie Academic&Professional, London, **1998**, pp. 251-277.

(21) J. Yu and R. Xu, *Chem. Soc. Rev.*, 2006, **35**, 593-604.

(22) J. Yu and R. Xu, *Acc. Chem. Res.*, 2003, **36**, 481-490.

(23) H. O. Pastore, E. C. de Oliveira and G. B. Superti, *J. Phys. Chem. C*, 2007, **111**, 3116-3129.

(24) M. Strauss, G. A. V. Martins, G. Berlier, S. Coluccia, L. Marchese and H. O. Pastore, *Microporous Mesoporous Mater.*, 2014, **187**, 135-144.

(25) X. Song, Y. Li, L. Gan, Z. Wang, J. Yu and R. Xu, *Angew. Chem. Int. Ed.*, 2009, **48**, 314-317.

(26) Y. Wang, J. Yu, Y. Li, Z. Shi and R. Xu, *Chem. Eur. J.*, 2003, **9**, 5048-5055.

(27) P. Chen, J. Li, J. Yu, Y. Wang, Q. Pan and R. Xu, *J. Solid State Chem.*, 2005, **178**, 1929-2934.

(28) X. Tong, W. Yan, J. Yu and R. Xu, *Chem. Commun.*, 2013, **49**, 11287-11289.

(29) N. Simon, T. Loiseau and G. Férey, *Solid State Sci.*, 2000, **2**, 389-395.

(30) V. A. Davankov, *Chirality*, 1997, **9**, 99-102.

(31) X. Bao, R. Q. Snurr and L. J. Broadbelt, *Microporous Mesoporous Mater.*, 2013, **172**, 44-50.

(32) T. Álvaro-Muñoz, F. López-Arbeloa, J. Pérez-Pariente and L. Gómez-Hortigüela, *J. Phys. Chem. C*, 2014, **118**, 3069-3077.

(33) B. Bernardo-Maestro, M. D. Roca-Moreno, F. López-Arbeloa, J. Pérez-Pariente and L. Gómez-Hortigüela, Catal. Today, 2016, **277**, 9-20.

(34) L. Gómez-Hortigüela, T. Álvaro-Muñoz, B. Bernardo-Maestro and J. Pérez-Pariente, *Phys. Chem. Chem. Phys.*, 2015, **17**, 348-357.

(35) B. Bernardo-Maestro, F. López-Arbeloa, J. Pérez-Pariente and L. Gómez-Hortigüela, *J. Phys. Chem. C*, 2015, **119**, 28214-28225.

(36) S. Qiu, W. Pang, H. Kessler and J.-L. Guth, *Zeolites*, 1989, **9**, 440-444.

(37) G. Férey, T. Loiseau, P. Lacorre and F. Taulelle, *J. Solid. State Chem.*, 1993, **105**, 179-190.

(38) F. Taulelle, T. Loiseau, J. Maquet, J. Livage and G. Fèrey, *J. Solid State Chem.*, 1993, **105**, 191-196.

(39) C. Schott-Darie, J. Patarin, P. Y. Le Goff, H. Kessler and E. Benazzi, *Microporous Mater.*, 1994, **3**, 123-132.

(40) S. J. Kirkby, A. J. Lough and G. A. Ozin, *Z. Kristallogr.*, 1995, **210**, 956.

(41) J. Renaudin and G. J. Férey, *Solid. State Chem.* 1995, **120**, 197.

(42) D. E. Akporiaye, H. Fjellvag, E. N. Halvorsen, T. Haug, A. Karlsson and K. P. Lillerud, *Chem. Commun.* 1996, 1553-1554.

(43) J.-L. Paillaud, B. Marler and H. Kessler, *Chem. Commun.* 1996, 1293-1294.

(44) S. F. Radaev, W. Joswig and W. H. Baur, *J. Mater. Chem.* 1996, **6**, 1413-1418.

(45) S. Oliver, A. Kuperman, A. Lough and G. A. Ozin, *J. Mater. Chem.* 1997, 7, 807-812.

(46) L. Schreyeck, P. Caullet, J. C. Mougenel, J. Patarin and J.L. Paillaud, *Microporous Mater.* 1997, **11**, 161-169.

(47) N. Simon, T. Loiseau and G. Férey, *J. Mater. Chem.* 1999, **9**, 585-589.

(48) W. Yan, J. Yu and R. Xu, *Inorg. Chem.* 2001, **40**, 379-383.

(49) P. S. Wheatley, C. J. Love, J. J. Morrison, I. J. Shannon and R. E. Morris, *J. Mater. Chem.* 2002, **12**, 477-482.

(50) L. A. Villaescusa, I. Bull, P. S. Wheatley, P. Lightfoot and R. E. Morris, *J. Mater. Chem.* 2003, **13**, 1978-1982.

(51) R. E. Morris, A. Burton, L. M. Bull and S. I. Zones, *Chem. Mater.* 2004, **16**, 2844-2851.

(52) N. Simon, J. Marrot, T. Loiseau and G. Férey, *Solid State Sci.* 2006, **8**, 1361-1367.

(53) P. S. Wheatley and R. E. Morris, *J. Mater. Chem.* 2006, **16**, 1035-1037.

(54) M. Zhang, D. Zhou, J. Li, J. Yu, J. Xu, F. Deng, G. Li and R. Xu, *Inorg. Chem.* 2007, **46**, 136-140.

(55) Y. Wei, Z. Tian, H. Gies, R. Xu, H. Ma, R. Pei, W. Zhang, Y. Xu, L. Wang, K. Li, B. Wang, G. Wen and L. Lin, *Angew. Chem. Int. Ed.* 2010, **49**, 5367-5370.

(56) P. Dauber-Osguthorpe, V. A. Roberts, D. J. Osguthorpe, J. Wolff, M. Genest and A. T. Hagler, *Proteins: Struct., Funct., Genet.* 1988, **4**, 31-47.

(57) L. S. Schanker, P. A. Shore, B. B. Brodie and C. A. M. Hogben, *J. Pharmacol. Exp. Ther.* 1957, **120**, 528-539.

(58) J. J. Williams, C. W. Smith, K. E. Evans, Z. A. D. Lethbridge, R. Walton, *Chem. Mater.* 2007, **19**, 2423-2434.

(59) Forcite module, Material Studio, BIOVIA, San Diego, CA, 2017.

(60) D. Zhou, J. Xu, J. Yu, L. Chen, F. Deng and R. Xu, *J. Phys. Chem. B* 2006, **110**, 2131-2137.

(61) L. Sierra, C. Deroche, H. Gies and J. L. Guth, *Microporous Mater.* 1994, **3**, 29-38.

(62) C. Martineau, B. Bouchevreau, R. Siegel, J. Senker, A. Ristić and F. Taulelle, *J. Phys. Chem. C* 2012, **116**, 21489-21498

(63) D. Wang, S. Xu, M. Yang, Y. Chu, P. Tian and Z. Liu, *J. Phys. Chem. C* 2016, **120**, 11854-11863.

(64) N. Zabukovec Logar, G. Mali, N. Rajic, S. Jevtic, M. Rangus, A. Golobic, V. Kaucic, *J. Solid State Chem.* 2010, **183**, 1055-1062.

(65) M. Strauss, G. A. V. Martins, G. Berlier, S. Coluccia, L. Marchese and H. O. Pastore, *Microporous Mesoporous Mater.* 2014, **187**, 135-144.

(66) H. O. Pastore, É. C. de Oliveira and G. B. Superti, *J. Phys. Chem. C* 2007, **111**, 3116-3129.

(67) N. Venkatathri, S. G Hegde, V. Ramaswamy and S. Sivasanker, *Microporous Mesoporous Mater.* 1998, **23**, 277-285.

(68) J.-S. Chen, W.-Q. Pang and R. Xu, *Top. Catal.* 1999, **9**, 93-103.

(69) J. Yu and R. Xu, *Chem. Soc. Rev.* 2006, **35**, 593-604.

(70) J. M. Thomas, R. H. Jones, R. Xu, J. Chen, A. M. Chippindale, S. Natarajan and A. K. Cheetham, *J. Chem. Soc. Chem. Commun.* 1992, 929-931.

(71) R. W. Dorner, M. Deifallah, D. S. Coombes, C. R. A. Catlow and F. Corà, *Chem. Mater.* 2007, **19**, 2261-2268.